Time-lapse full-waveform inversion as a reservoir-monitoring tool — A North Sea case study

Erik Hicks[1], Henning Hoeber[1], Marianne Houbiers[2], Séverine Pannetier Lescoffit[2], Andrew Ratcliffe[1], and Vetle Vinje[1]

Abstract

Full-waveform inversion (FWI) has become an enabling tool for 3D velocity-model building, especially in the shallow part of the seismic image that is well probed by diving waves. Given that FWI provides direct access to P-wave velocities, its application to time-lapse (4D) studies is of obvious interest. Can 4D FWI give fast access to small reservoir production-related velocity changes and compete with traditional 4D time-shift results based on fully processed and imaged reflection data? Also, what algorithmic developments may be needed to achieve robust 4D FWI results? Time-lapse data sets acquired with highly repeatable permanent-reservoir-monitoring (PRM) acquisition systems, such as the one deployed over the Grane Field in the Norwegian North Sea, are well suited to help address these questions. We demonstrate the success of the 4D FWI technique using a synthetic study involving 3D elastic modeling through a highly realistic earth model akin to the actual Grane PRM data. This study indicates there is minimal sensitivity of the method to various residual uncertainties in the data and in the modeling for this acquisition configuration. The 4D FWI results using real time-lapse Grane PRM data acquired in the field with a six-month acquisition interval between vintages show changes at the reservoir level that correlate with both injecting and producing wells. We also find good agreement when comparing the velocity differences from 4D FWI to 4D time shifts and time strains from the fully processed and imaged seismic reflection data. Given that the FWI updates are driven mainly by diving waves, whereas the time-strain analysis uses reflection data, this gives increased confidence in both sets of results. Overall, this case study demonstrates the potential of FWI as a reservoir-monitoring tool.

Introduction

Full-waveform inversion (FWI) has the ability to use acquired seismic data to recover the physical earth parameters that affect the seismic wavefield directly (Tarantola, 1984). Such schemes solve an optimization problem in which acquired data are compared, in an iterative manner, to synthetic data obtained from wave-equation modeling. The information in this comparison then provides an update to the earth model. In practice, we often need to make approximations to keep computational costs under control. In particular, full elastic-wave propagation and attenuation effects are seldom included in industrial-sized FWI applications, and the data are commonly modeled using the acoustic-wave equation.

In recent years, the use of a diving-wave-driven FWI to invert for P-wave velocity, V_P, in the context of improving the velocity model and subsequent prestack depth migration (PSDM) has become common practice. By contrast, real-data case studies (as opposed to synthetic-data tests) of FWI in a time-lapse (4D) setting are still exceedingly rare (exceptions are Raknes et al., 2013 and Chen et al., 2015), despite the obvious potential to (rapidly) deliver high-resolution velocity changes due to production effects between a baseline seismic and subsequent monitor data set.

Several authors have proposed a number of schemes and cost functions to perform 4D FWI, often depending on their assumptions about the potential repeatability of the acquisition. These include parallel schemes, where the inversion is run once on each vintage in full, and the base and monitor models are subtracted (Plessix et al., 2010). Coupled schemes, with names such as cascaded (Asnaashari et al., 2012; Routh et al., 2012) and double-difference (Watanabe et al., 2004; Denli and Huang, 2009; Zheng et al., 2011), attempt to introduce into the inversion some degree of 4D coupling between vintages. Joint 4D cost functions also have been suggested (Maharramov and Biondi, 2014), as has the use of inversion constraints, such as regularization schemes and inversion masks (Asnaashari et al., 2015). Tests and comparisons of these schemes on synthetic data tend to give conflicting conclusions depending on the synthetic example being studied and whether or not perfect acquisition repeatability is assumed. Overall, the situation does not seem conclusive yet, and more real-data testing is clearly needed.

Our data set for 4D FWI comes from the relatively shallow Grane heavy-oil field in the Norwegian North Sea. A seabed-based permanent-reservoir-monitoring (PRM) system was installed in 2014, and the first two vintages of PRM data are used in this study. PRM data sets should be ideal for 4D FWI due to their excellent repeatability and the availability of long offsets, good azimuth coverage, and low frequencies. That said, even here the success of a 4D FWI scheme is by no means guaranteed: the PRM data acquisitions are frequent; the 4D effects are small and complex; and, while the repeatability is very high, in reality it will never be perfect.

To gain more experience using FWI in a relevant 4D setting, we start our study with synthetic modeling and algorithmic testing based on the Grane acquisition setup. A 3D elastic model is constructed using a depth-imaging velocity model, and a time-lapse model is built using actual Grane reservoir model data. With the elastic synthetic time-lapse data, we can investigate different 4D FWI schemes as well as the influence of using an acoustic (rather than elastic) inversion scheme in a similar setting to the real Grane PRM data. Exhaustive testing of the various 4D FWI schemes mentioned above is clearly resource intensive. Hence, after some preliminary internal 2D testing of the majority of these schemes, we consider in this paper only two 4D FWI schemes in detail. First, to establish a benchmark 4D result, we use the straightforward parallel flow, whereby base and monitor are inverted on their own, starting from the same initial model. Then, we show the results of a new scheme, where base and monitor inversions ultimately are coupled through the use of a common starting model. We highlight that the results shown here represent the project's current status, with further improvements and answers likely in the future.

The Grane Field

The Grane Field is located in the Norwegian North Sea, in ~125 m water depth. The reservoir consists of Heimdal sands at a fairly constant depth of ~1750 m (Sinha Roy et al., 2011). Grane is a heavy-oil field, with no initial gas cap. The sands have a low initial P-impedance contrast to the surrounding Lista shales, which makes mapping using reflection (PP) data difficult. The sands can be identified more readily on converted-wave (PS) seismic data, while production effects are visible on PP seismic data due to saturation changes and gas injection. The reservoir overlies a rugose high-velocity chalk layer that creates challenges for many aspects of seismic data processing. The overburden contains high-velocity consolidated sand bodies that distort deeper seismic events. The field was discovered in 1991, and production began in 2003 with a 4D monitoring program in place since 2005 using towed-streamer acquisitions every second year. The PRM system installed in 2014 consists of 3300 receivers (spacing 50 m) trenched into the seabed on 17 parallel lines that are 300 m apart, covering approximately 50 km² (Thompson et al., 2015). Four vintages of PRM data have been acquired so far, namely the base (PRM0) and three monitor surveys (PRM1, PRM2, and PRM3), acquired at six-month intervals (Sinha Roy et al., 2015; Elde et al., 2016). For PRM0 and PRM1, shots are on a 50 × 50 m flip-flop preplot distribution extending 3 km beyond the receiver patch, nominally giving ~66,000 shots (Figure 1). Shot coverage is reduced slightly for PRM2.

Synthetic 4D FWI study

To investigate the feasibility of FWI as a tool for reservoir monitoring, we need a realistic synthetic data set generated under controlled conditions. Hence, we create base and monitor surveys using 3D elastic finite-difference (FD) forward modeling. Realistic production effects, extracted from the existing reservoir model, are included in the monitor model (Lescoffit et al., 2016). A vertical transverse isotropic (VTI) PSDM model derived from reflection tomography is used as a starting point in this process, consisting of V_P, V_S, and Thomsen's (1986) anisotropy parameters ε and δ. One problem we encountered is that this PSDM imaging model is too smooth to provide realistic reflections in the FD modeling. We overcome this by adding appropriately scaled high-frequency perturbations to the V_P model that are computed from a 1D acoustic impedance inversion of the real seismic reflection data, with the scaling obtained by comparison to existing well logs. Gardner's relation (Gardner et al., 1974) is used to generate the base density model. The detailed V_S model is created by applying the local V_P/V_S ratio from the original PSDM model to the detailed V_P model. Figure 2 shows the V_P and V_S base models before and after addition of the high-frequency details to form the final synthetic models used in this study. Given that 3D FWI is a CPU- and time-intensive process, 2D elastic modeling and FWI on a single line extracted from the synthetic models are used to perform some investigations to narrow down the number of workflows to be tested in 3D and as a tool to quickly test other assumptions. However, we emphasize that all the displays in this paper come from a full 3D/4D analysis and highlight that, whenever we comment on results from these 2D tests, we clearly state this fact.
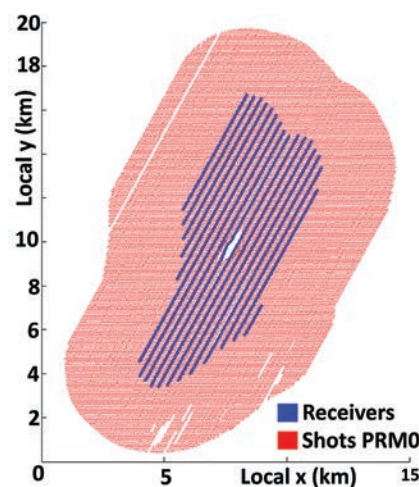

Figure 1. The Grane PRM survey layout (from Lescoffit et al., 2016). The 17 receiver lines, 300 m apart, are shown in blue, and the shot coverage is displayed in red. The shooting vessel safety zone around the Grane platform is visible as the hole in the center of the shot acquisition.

The time-lapse model consists of four separate effects (Lescoffit et al., 2016):

- a water-velocity change near the sea surface based on real water-velocity profiles measured during acquisition
- local V_P effects resembling a waste injector in the overburden
- broad-scale stress effects in the overburden ($\Delta V_P < 5$ m/s)
- production-related changes to all of V_P, V_S, and ρ in the reservoir

For the latter item, the reservoir production effects are separated spatially into a weak (two years of production) and a strong (10 years of production) effect, with half of the reservoir having the weaker 4D signal (the right-hand side of Figures 3a and 3c).

To conduct this elastic modeling study of 66,000 shots in a realistic timeframe, we use reciprocity and model 3300 receiver gathers instead. Although reciprocity does not hold strictly for elastic modeling when sources are close to the seabed, tests show that the errors are small and confined to the converted wave energy. The receiver positions are assumed to be identical for base and monitor, as the real PRM receivers are trenched into the seabed. Both the base and monitor survey modeling generate synthetic data using the actual field-acquisition preplot shot positions. In addition, as the full wavefield is modeled, data also can be output at the true field shot locations with minimal overhead. This was done for the monitor data set to evaluate the effect of realistic acquisition nonrepeatability. The 3D elastic modeling is performed to a maximum frequency of 15 Hz, with a source wavelet estimated from the real data and a free surface in the modeling to generate the surface multiples and ghosts that we expect in the real data. The elastic modeling code uses a highly accurate FD scheme based on the Lebedev staggered grid (Lebedev, 1964; Lisitsa and Vishnevskiy, 2010) and a fourth-order stepping in time (Etgen, 1986). No noise was added to the synthetic data.

We outline the *acoustic* 4D FWI workflow for V_P based on these *elastic* base and monitor data sets. In addition to the acoustic/elastic difference, we highlight that our acoustic FWI uses a different FD scheme to the elastic modeling, meaning we do not perform the "inverse crime" of using the same modeling engine to both create and invert the data. A smoothed version of the

PSDM V_P model is used as the starting model for both data sets — this is appropriate for this work as reflection tomography in the real-data case is expected to generate a starting model that does not lead to cycle skipping between the real and modeled data. Also, ray tracing indicates that the diving waves, which drive the FWI, in the acquired offset range should penetrate at
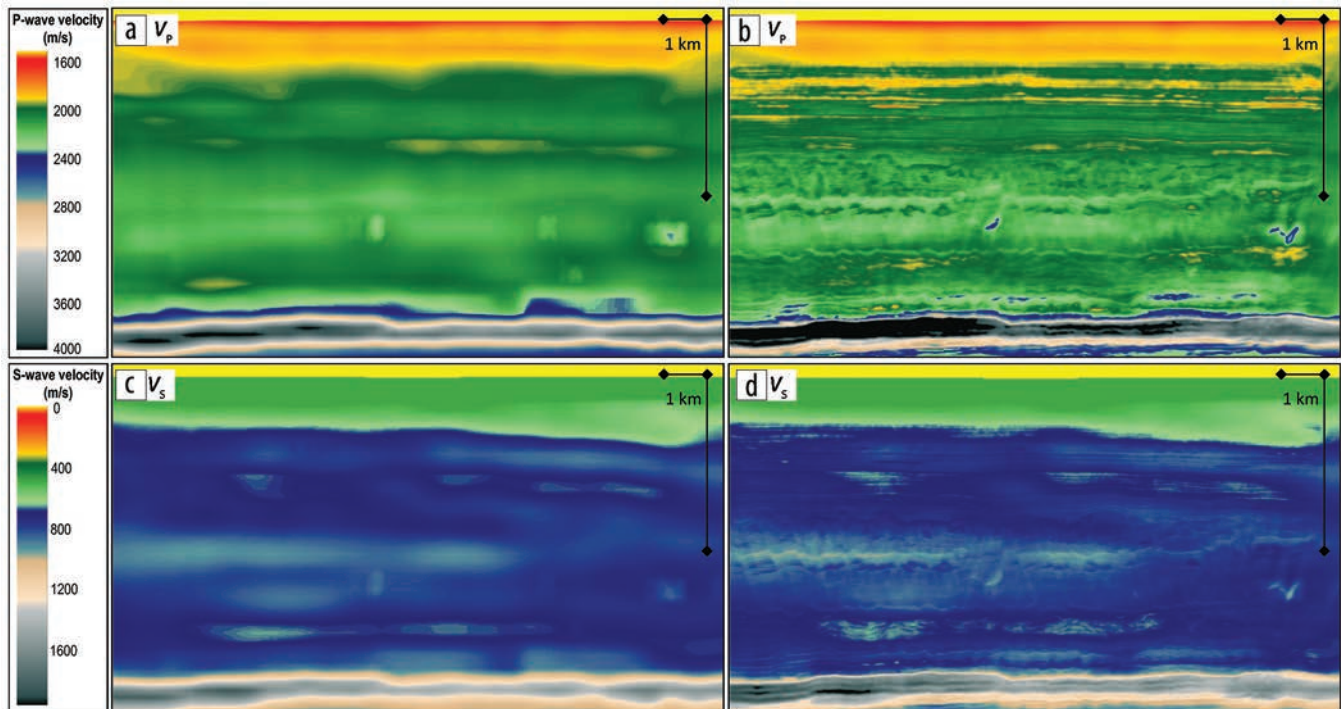

Figure 2. Derivation of the synthetic models on inline sections: (a) V_P PSDM imaging model; (b) final V_P base model created by adding high-frequency details from a 1D impedance inversion; (c) V_S PSDM imaging model; and (d) final detailed V_S base model.
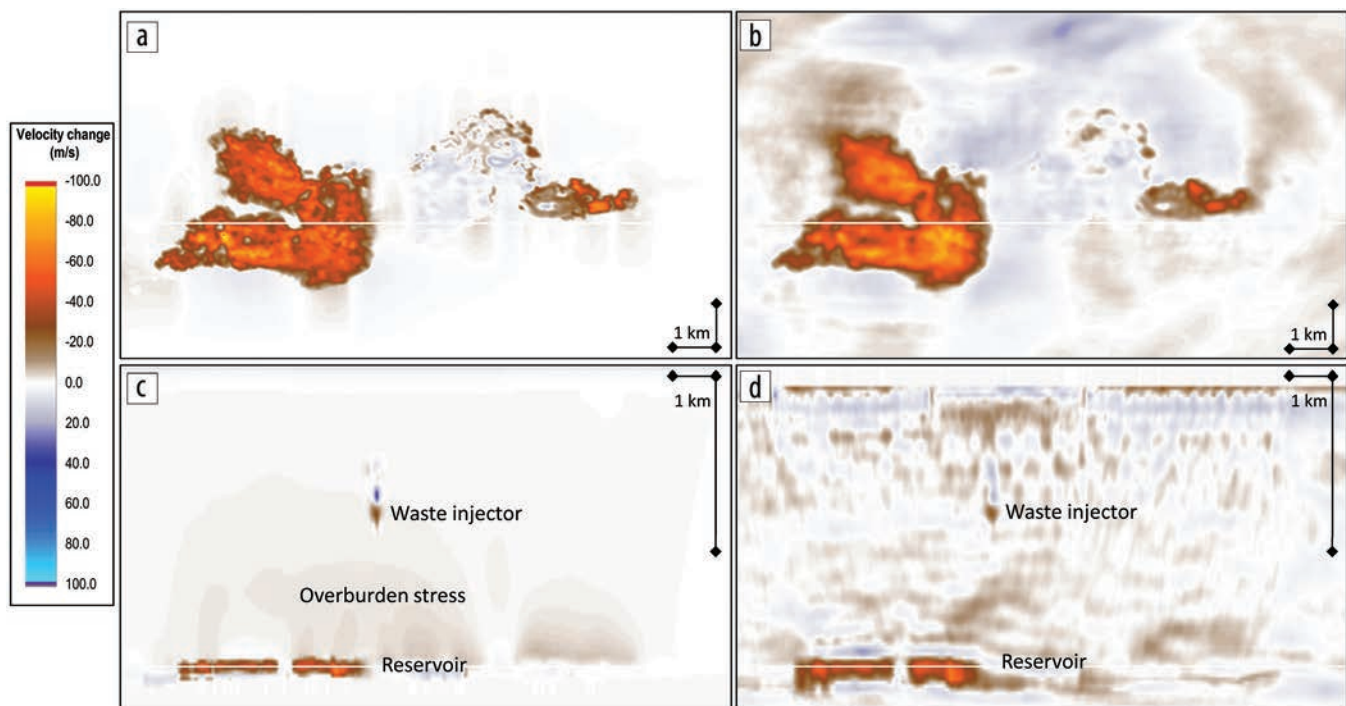

Figure 3. Results from the synthetic study: (a) ΔV_P reference and (b) parallel 4D FWI result at 11.8 Hz on a depth slice at the reservoir level; (c) ΔV_P reference and (d) parallel 4D FWI result at 11.8 Hz on a vertical section at the location of the waste injector in the overburden. The thin white line on the depth slices in (a) and (b) indicates the position of the vertical section, and vice versa with (c) and (d).
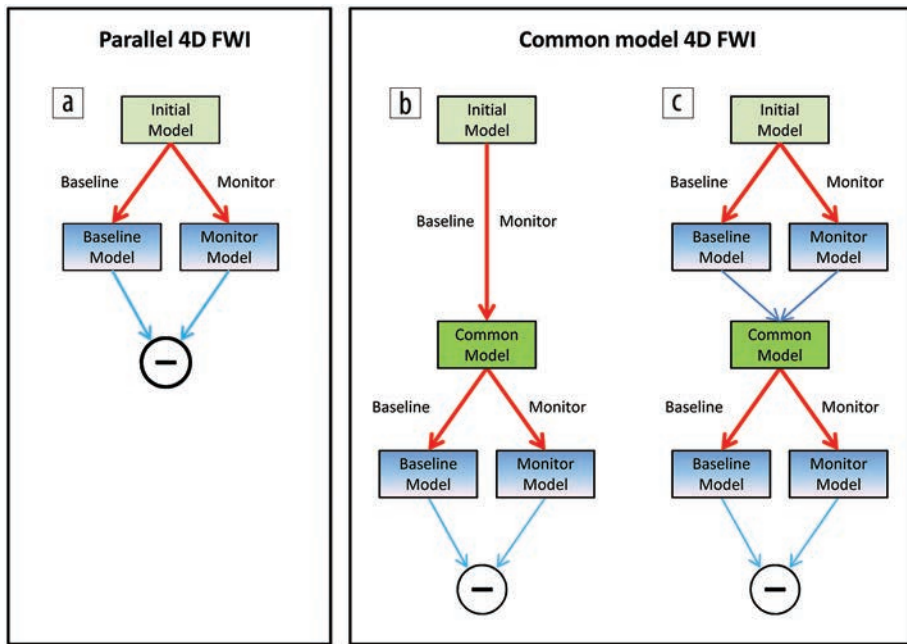
Figure 4. Comparison of 4D FWI workflows: (a) Parallel and (b) and (c) the two common-model schemes. In this display, boxes represent velocity models and red arrows are the FWI process applied in one or more frequency bands. Note how the first inversions of (c) common-model scheme are identical to (a) the parallel case.

One potential issue we did not test is the sensitivity to errors in the source wavelet. Ideally, acquisitions for 4D will use an identical source signature for all the vintages; however, this sometimes may not be possible for operational reasons.

Common-model 4D FWI

Parallel 4D FWI is a straightforward scheme that has the benefits of not requiring repeatable acquisition, or any new algorithmic development, while allowing various post-FWI processing steps to be applied to each vintage's result if needed (such as footprint attenuation). However, it has some obvious limitations: it assumes similar levels of convergence between vintages, with such convergence depending on data quality and FWI parameters used, and also that corresponding minima in the cost function are found by each inversion. The former point is likely to be more controlled in this work due to the PRM nature of the data set and sensible choices for the FWI parameters. The latter point is more problematic and is driven by *any* differences in the acquisition, for example, different shot positions, source signatures, weather conditions, water-column changes, ambient noise, etc. It is also influenced by how acoustic FWI deals with the unfittable parts of the real data (for example, due to elastic effects). The large dimensionality and nonlinear nature of FWI means that these changes almost guarantee different local minima will be obtained when inverting different vintages. All of these effects will cause additional noise in the 4D FWI analysis. But, such behavior does not automatically render 4D FWI analysis futile, as this noise is not guaranteed to swamp the 4D signal.

With these thoughts in mind, we highlight two ideas that have been proposed to stabilize 4D FWI. First, masking is sometimes used in elastic AVO inversions, where prior knowledge about the size and location of the 4D effects is used to constrain model parameters. Masking also has been suggested in the 4D FWI context (Zhang and Huang, 2013) and seems a sensible way to focus on the 4D changes. However, our a priori knowledge of the 4D changes is generally limited, and we certainly do not wish to constrain the inversion in the overburden. Hence, the most we want to do is mask spurious 4D effects below the reservoir, which, in our case, means below the top chalk. Second, can coupling the inversions help? Some existing methods to introduce coupling have inherent challenges. Cascaded 4D FWI, where the final model obtained from one vintage is used as a starting model for the second vintage, assumes complete and stable convergence, with additional iterations in the first vintage yielding zero updates to the base model result. In reality, this is never the case within a reasonable timeframe (if at all), so potentially large 4D differences tend to be introduced between the data sets because one vintage has a different convergence level compared to the other vintage.
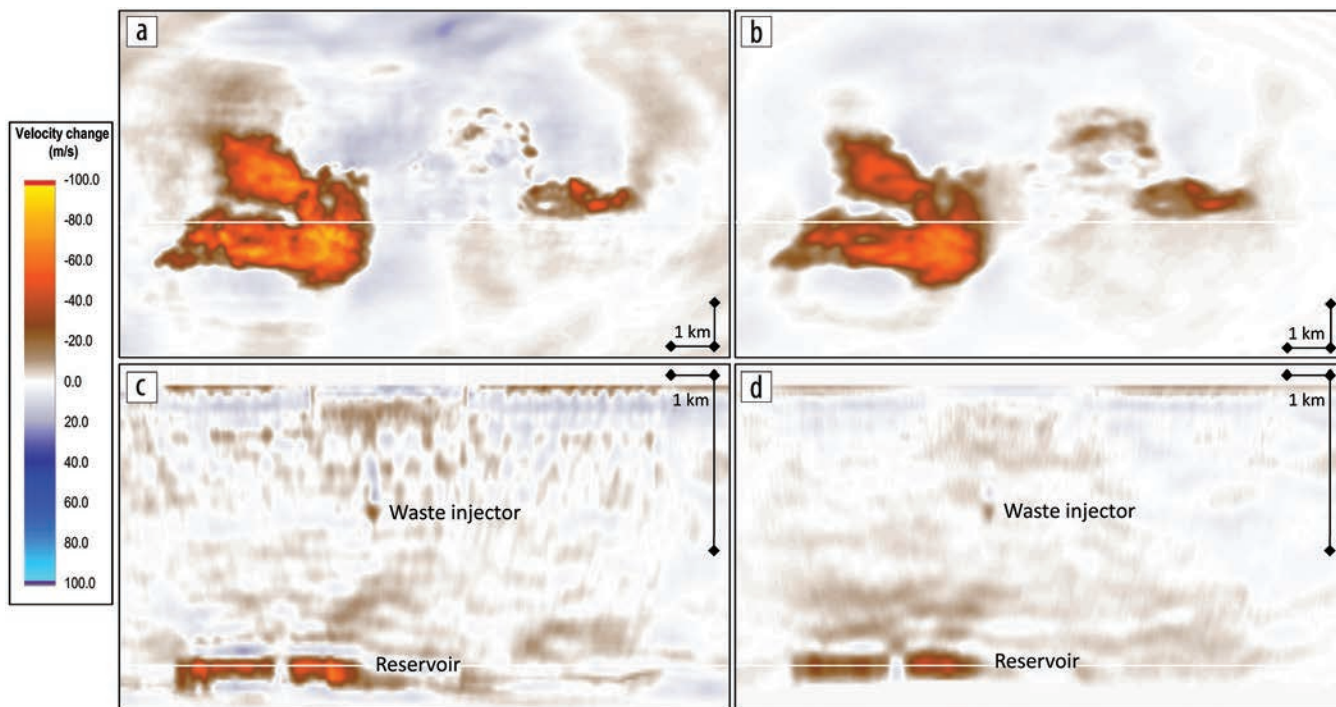
least down to the level of the top chalk — i.e., they probe the reservoir level. The first iterations are limited to the lowest frequencies (4.2 Hz) and are gradually increased up to 11.8 Hz.

Twelve iterations are run in each of seven different frequency bands. Initially, base and monitor data sets are inverted in a fully parallel fashion (see workflow in Figure 4a). As we are interested in determining the stability of the FWI process, no constraints are placed on the inversion at this time. Results are shown in Figure 3 and compared to the known "true" model. By definition, any difference in the 4D FWI-inverted V_p that is not in the models is noise: we observe strong noise near the seabed, but moderate at reservoir depth (Figure 3d). FWI is able to recover the reservoir production effects and the overburden injector with reasonable accuracy, albeit with lower resolution compared to the true model because of the limited maximum frequency used. The broad-scale, low-magnitude velocity change in the overburden due to stress arching could not be identified over background noise.

So far, the synthetic data tests have used ideal base and monitor PRM acquisition geometry with perfectly colocated shots. A test using the true field shot positions to introduce realistic positioning differences between vintages showed minimal added noise in the parallel 4D results, apart from areas containing significant acquisition differences due to infrastructure changes in the area (rig holes) or missing sail-line segments, etc.

For this particular PRM acquisition setup and reservoir setting, the synthetic study implies that several potential issues do not cause significant problems for 4D FWI, although they may introduce additional noise into the result:

- accoustic inversion assumption applied to elastic data
- minor water-velocity differences
- minor acquisition repeatability differences (e.g., shot-positioning errors, generally below 25 m)

Figure 5. Results from the synthetic study: (a) ΔV_p for parallel 4D FWI at 11.8 Hz and (b) common-model 4D FWI at 14 Hz on a depth slice at the reservoir level; (c) parallel 4D FWI at 11.8 Hz and (d) common-model 4D FWI at 14 Hz on a vertical section at the location of the waste injector. Note the reduction in noise in the common-model result away from the areas of true 4D signal. The thin white line on the depth slices in (a) and (b) indicates the position of the vertical section, and vice versa with (c) and (d).

The double-cascaded approach attempts to overcome this issue at the cost of more passes through the vintages (Maharramov and Biondi, 2014). The double-difference method (Watanabe et al., 2004; Denli and Huang, 2009; Zheng et al., 2011) tries to overcome the generation of spurious model perturbations by constructing a new data set for the inversion where the 4D difference between real data sets is added to the appropriately scaled modeled data generated from the final iteration of the base FWI model. Hence, the double-difference method requires obtaining the correct scaling for the modeled data (potentially a nontrivial task), ideally with the same source signature in all vintages, as well as having colocated data between the vintages. Colocation is obviously trivial for synthetic data; however, in the real world, it means applying data regularization to at least one vintage. This regularization process is itself not without potential issues and, if our aim is a (relatively) fast and simple 4D inversion scheme with minimal processing, then this scheme could be too complex.

Given the complications discussed in the previous two paragraphs, we propose a new method of coupling several vintages of seismic data for FWI — we call it the common-model scheme. We start by deriving a velocity model that is applicable as an appropriate (converged) starting model for all vintages. This is determined at a high upper-frequency limit, so that the solution will not be cycle skipped or fall into local minima due to differences between vintages, or generate the spurious model perturbations discussed above. This common model then becomes the starting point for running (parallel) high-frequency FWI iterations in each vintage. The common starting model can be created by running the full FWI flow from low to high frequency using an input data set consisting of all vintages merged.

Alternatively, an average (in slowness) of models after a low- to high-frequency parallel 4D FWI can be used. A schematic view of these workflows is shown in Figure 4. Two-dimensional tests with synthetic data showed only minor differences between these two approaches. Therefore, for the 3D synthetic study we average the models after parallel FWI as this is clearly more efficient, having already generated these results. Hence, the models created after FWI at 11.8 Hz on the synthetic data sets are combined and 12 iterations run at the final frequency band of 14 Hz. A comparison of the results from synthetic testing using the parallel and common-model 4D FWI schemes is shown in Figure 5. The 4D effects are displayed after 12 iterations at 11.8 Hz for the parallel flow and continued to 14 Hz for the common flow. Clearly, the noise level outside the true 4D signal areas in the common scheme is reduced compared to the parallel scheme. The 4D difference in the common model was still developing at the 12th iteration, so the resolution and absolute values are slightly low compared to the true difference, and it is likely that further iterations would improve this result.

In a comparison with the other semicoupled methods mentioned earlier, 2D synthetic tests showed that the common-model approach is more robust and slightly less noisy. The common scheme, by its nature, is better suited to 4D differences that are small enough to not introduce cycle skipping within the frequency band of interest. It should work well for the Grane PRM data, with anticipated 4D velocity changes of up to 2%. When FWI is run coupled via the common starting model and using the maximum frequency range, noise that would otherwise accumulate through iterations/frequency bands is attenuated, giving a cleaner 4D result. Any wavelet differences between data sets need to be

known and compensated either before or during inversion to reduce the risk of the algorithm finding different local minima in the cost functions. This is perhaps more critical compared to parallel FWI, as the common-model FWI starts at a higher frequency.

4D FWI using real Grane PRM data

The 4D FWI results from the elastic synthetic study are sufficiently encouraging to justify proceeding with a real-data test using the first two vintages of the Grane PRM data. During interpretation of the conventional 4D imaging products, two fairly strong gas effects were identified on the final images of the reflection seismic: a gas injector near the edge of the survey patch and a gas-cap expansion associated with a producing well near the central platform. In addition, several zones of smaller and noisier time shifts and time strains that correlate with the well tracks are also visible (see Figures 9c–f).

The estimated ΔV_P based on time shifts observed in the reflection data is of the order of 50–100 m/s, making these two data sets good candidates for 4D FWI. Unfortunately, for reliability

Figure 6. An example of a PRM0 receiver gather (one sail line), with the mutes used to highlight the first arrival, diving-wave energy in FWI shown as yellow lines. A 14 Hz low-pass filter is applied, in addition to the 3 Hz acquisition low-cut.

reasons, a reconfiguration of the source had to be performed between the two acquisitions, creating some source differences between the two vintages. The source signature of each vintage is estimated from 4C data based on up/down separation (PZ summation) and receiver deghosting over a number of near-offset traces (Westerdahl, personal communication, 2015). They appear to capture most of the differences in the wavelets, allowing them to be included in the FWI modeling. As is typical for our FWI workflow, data preprocessing is minimal, and we only want to remove energy that is not modeled by the acoustic wave equation. Thus, only random noise and seismic interference attenuation are applied. Preprocessing specific to 4D is limited to shot and receiver synchronization; only receivers common to both data sets are kept, and shots with position differences greater than 25 m between acquisitions are dropped from both vintages. For these two vintages, the latter corresponds to 0.3% of the total number of traces being removed. No regularization, water-column corrections, or tidal-static corrections are applied. Also, no other a priori information (well data, constraints, masks, etc.) is included in the inversion, except for a constant-depth, linear taper of the update back to the starting model below the reservoir.

Previously, 3D FWI has been run on the first vintage of PRM data to generate an accurate velocity model for depth imaging (Lescoffit et al., 2016). Data input to 3D FWI excludes offsets below 1000 m and has a fairly tight mute applied to highlight the diving waves. The same mutes are also used in the 4D FWI workflow (Figure 6). The final 3D FWI imaging model (inverted up to 11.8 Hz) was smoothed slightly and used as a starting model for 4D FWI. As this 4D starting model is well suited for FWI (being itself a result of FWI), the 4D inversions could start with no maximum offset limit and a relatively high starting frequency of 7 Hz. Twelve iterations are run in each of five frequency bands up to 14 Hz in parallel flows, i.e., with no coupling between the base and monitor.
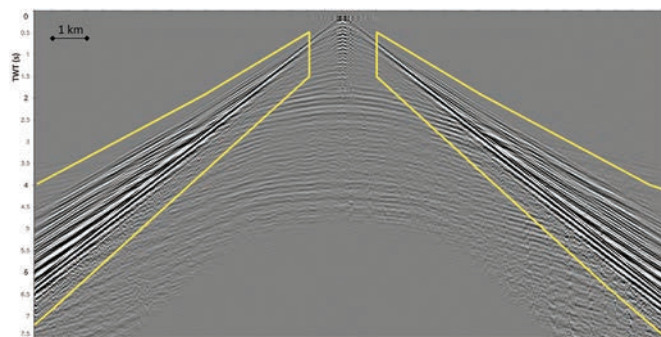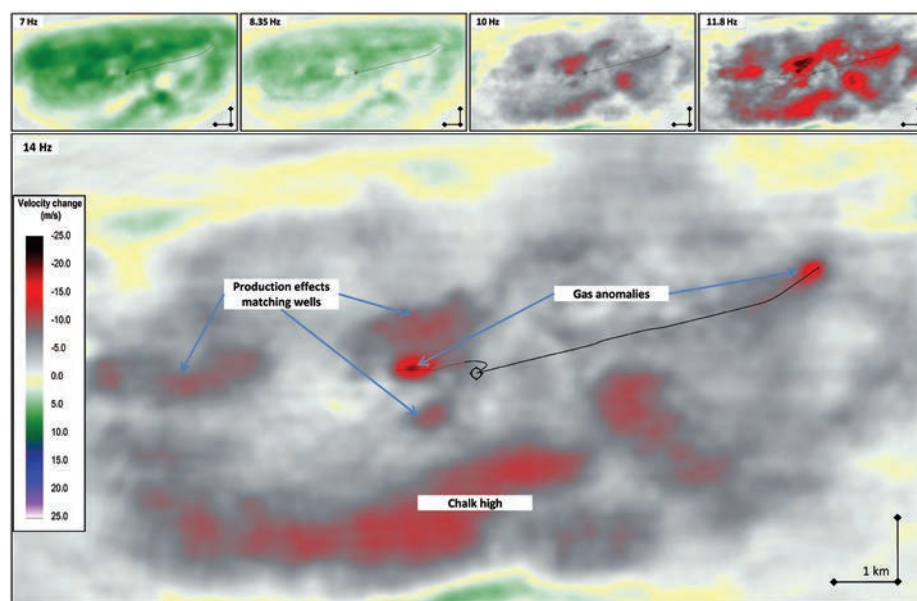
Figure 7 shows the results of the 4D model difference from the parallel inversions on a depth slice at the reservoir level. The two expected gas effects are visible (weakly at 7 Hz, reasonably clearly from 8.35 Hz onward). As a guide to the eye, the well paths related to the two gas effects are plotted. At 14 Hz, the two gas anomalies are clearly defined as decreases in velocity of ~25 m/s. This represents a velocity change of ~1%. Further work may be required to show if the velocities are fully converged at these frequencies. The Grane reservoir is located above a chalk layer with a very strong velocity increase compared to the surrounding sediments. This velocity increase is affecting the 4D FWI, causing a large false anomaly (noise) in the depth slice at the reservoir level along a chalk high. Also highlighted on Figure 7 are three other areas

Figure 7. Results from the Grane PRM real-data study: parallel 4D FWI results shown as velocity changes (ΔV_P) from base to monitor on a depth slice at the reservoir level. The intermediate inversions at lower frequencies are shown at the top. The color scale is the same for all displays (± 25 m/s), with red/black representing a decrease in velocity. Well paths associated with the two gas anomalies are shown.

outside the chalk high which show a weaker velocity decrease.

Using the real data, we mirror the workflow applied to the synthetic data sets to create a common-model 4D FWI. The 14 Hz models from the parallel inversions are combined to create the common model. We then continue to invert both base and monitor at 14 Hz. However, the results contain a large amount of leakage associated with geology, most visibly from the chalk, in the 4D difference, implying that some unaccounted difference between the data sets is causing the inversion to introduce different geologic updates. A possible explanation is the residual wavelet differences between the two vintages that are not fully compensated in the signature estimations. Therefore, we tested the common-model FWI at lower frequencies (using the same starting model) and found that 10 Hz gives a more stable result, with reduced noise compared to the parallel case (Figure 8). Interestingly, the recovered values of ΔV_P are higher than with the parallel scheme, even after just 12 iterations. (Obviously, the 4D differences before the first iteration here are zero by construction of the common model.) The peak ΔV_P is -35 m/s in the central gas anomaly after the common-model update, compared to -20 m/s and -25 m/s after the 10 Hz and 14 Hz parallel scheme, respectively. Thus, the
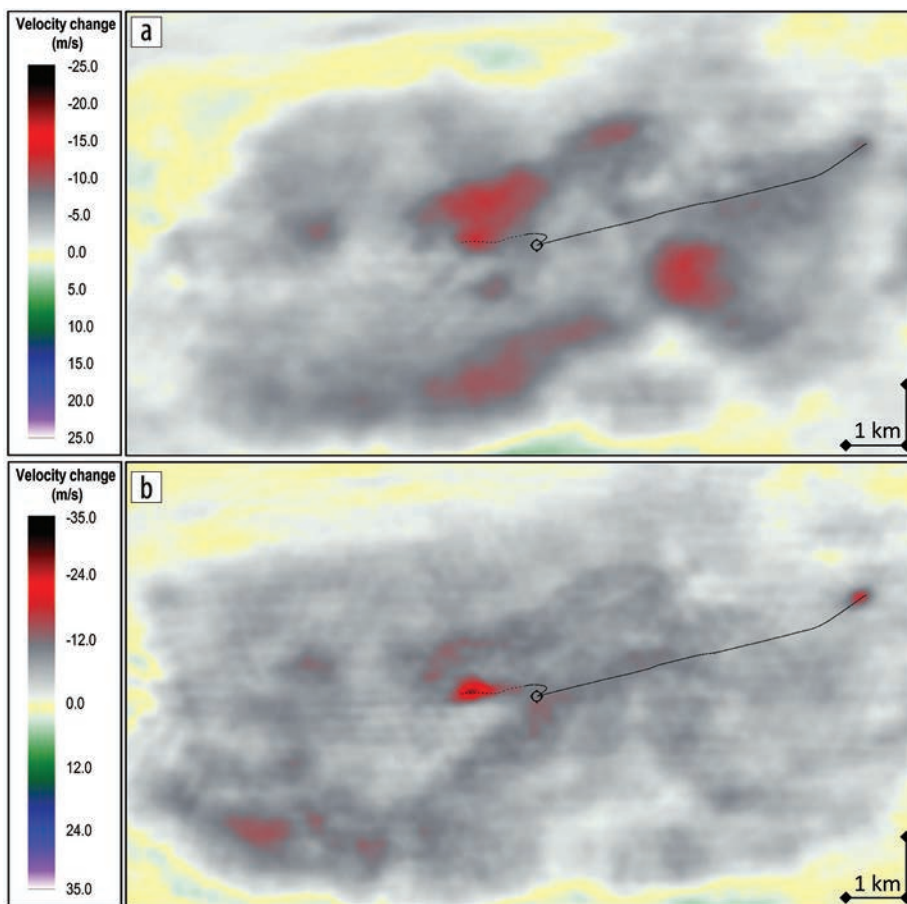

Figure 8. Results from the Grane PRM real-data study. Velocity changes from base to monitor on a depth slice at reservoir level for: (a) parallel FWI at 10 Hz and (b) common-model FWI at 10 Hz. Note the different ranges in the color scales between these two displays. The common-model update has recovered higher values of ΔV_P in the gas anomaly locations and the noise from the chalk high is reduced. Well paths associated with the two gas anomalies are shown.

10 Hz common-model results are closer to the velocity change predicted by time shifts. This raises the question: what is the optimal frequency to introduce coupling by combining models from parallel FWI? Although these initial results from the common-model update are exciting, further work is required to optimize this workflow when applied to real data.

Finally, we compare the 4D velocity changes from the common-model 4D FWI with the time strains derived from conventional 4D processing. This will give an indication as to whether or not diving waves have the same sensitivity to production-related changes as reflection data. For the time-strain analysis, time shifts and their derivatives with respect to time are simultaneously inverted by minimizing the difference between the base at two-way time, t, and the monitor at two-way time, $t + \tau(t)$, ignoring amplitude changes. We increase spatial consistency and temporal smoothness of the time strains by using small spatial operators and a regularization scheme for smooth time-shift derivatives. If $\tau(t)$ denotes the accumulated 4D time shift and Δt is a layer (interval) time shift, then

$$\frac{\partial \tau}{\partial t} = \frac{\Delta t}{t}. \tag{1}$$

The fractional change in traveltime across a layer $\Delta t/t$ is often called the time strain (Hatchell and Bourne, 2005). These traveltime changes are related to changes in layer thickness and velocity (via $v = z/t$) through

$$\frac{\Delta t}{t} = \frac{\Delta z}{z} - \frac{\Delta v}{v}. \tag{2}$$

Ignoring layer compaction, $\Delta z/z$, we see that time strains and relative interval velocity changes are of equal magnitude and opposite sign.

Figure 9 shows the comparison on a depth slice and vertical section of the relative velocity change obtained with FWI and the time-strain calculation obtained from the fully processed and imaged reflection data. Qualitatively, production effects seen on the 4D FWI are consistent with the time shifts and time strains extracted from the reflection data, albeit weaker. They correspond to expected effects of hydrocarbon production at specific well locations. Also, compared to the 4D FWI result, we see that the time strains are noisier. This is partially due to algorithmic noise, as we are calculating a derivative, and partially due to noise in the data,

for instance, due to reduced fold in the platform shadow zone. An additional point worth considering is that to extract time shifts and time strains from reflection data, acoustic impedance contrasts must exist; areas of low reflectivity will be subject to higher levels of noise and consequently larger uncertainties. The FWI results, relying primarily on diving waves propagating laterally in the subsurface, are largely unaffected by these issues.

It is uncertain whether the leakage from the high-velocity chalk layer in the 4D FWI observed in the parallel and 14 Hz common model is an effect of residual wavelet differences caused by the change in source from base to monitor, or whether the strong impedance contrast itself has a detrimental effect on the stability of the inversion. Quantitatively, velocity changes predicted by time shifts in the reflection stack are somewhat higher (up to three times) compared to the parallel 4D FWI results. Both of these points are subject to future investigation. However, we would like to emphasize that subsequent vintages of Grane PRM data will use a consistent seismic source configuration, thus eliminating the potential instability we see here caused by residual source signature errors between the first two vintages.

Overall, the results from the 4D FWI and the 4D time strains are remarkably consistent. This provides additional verification that the 4D processing of the PRM reflection data has preserved the production effects present in the raw data. Only further work will show how FWI inversion using diving waves and time-strain inversion using reflection data can complement each other in an integrated 4D flow: which one has higher resolution, which has less uncertainty, and which can be delivered with the shortest turnaround?

Conclusions

We have performed a 4D FWI study using field data from two vintages of the Grane PRM system located in the North Sea. Given these high-quality, well-repeated data, we show that current FWI implementations can reliably recover P-wave velocity changes related to gas replacing oil in hydrocarbon production at Grane, even over relatively short time intervals. Both a basic parallel and a new common-model 4D FWI scheme show 4D velocity changes in the field data, but noise is better suppressed in the new coupled scheme. The observed changes at the reservoir level correlate well with gas replacing oil effects due to injection and production at well locations. These 4D FWI results, mainly driven by diving waves, tie with those from time-strain analysis driven by reflection data. This provides increased confidence in both results. This case study demonstrates the effective use of FWI in a time-lapse application. To the best of our knowledge, this link (and agreement)
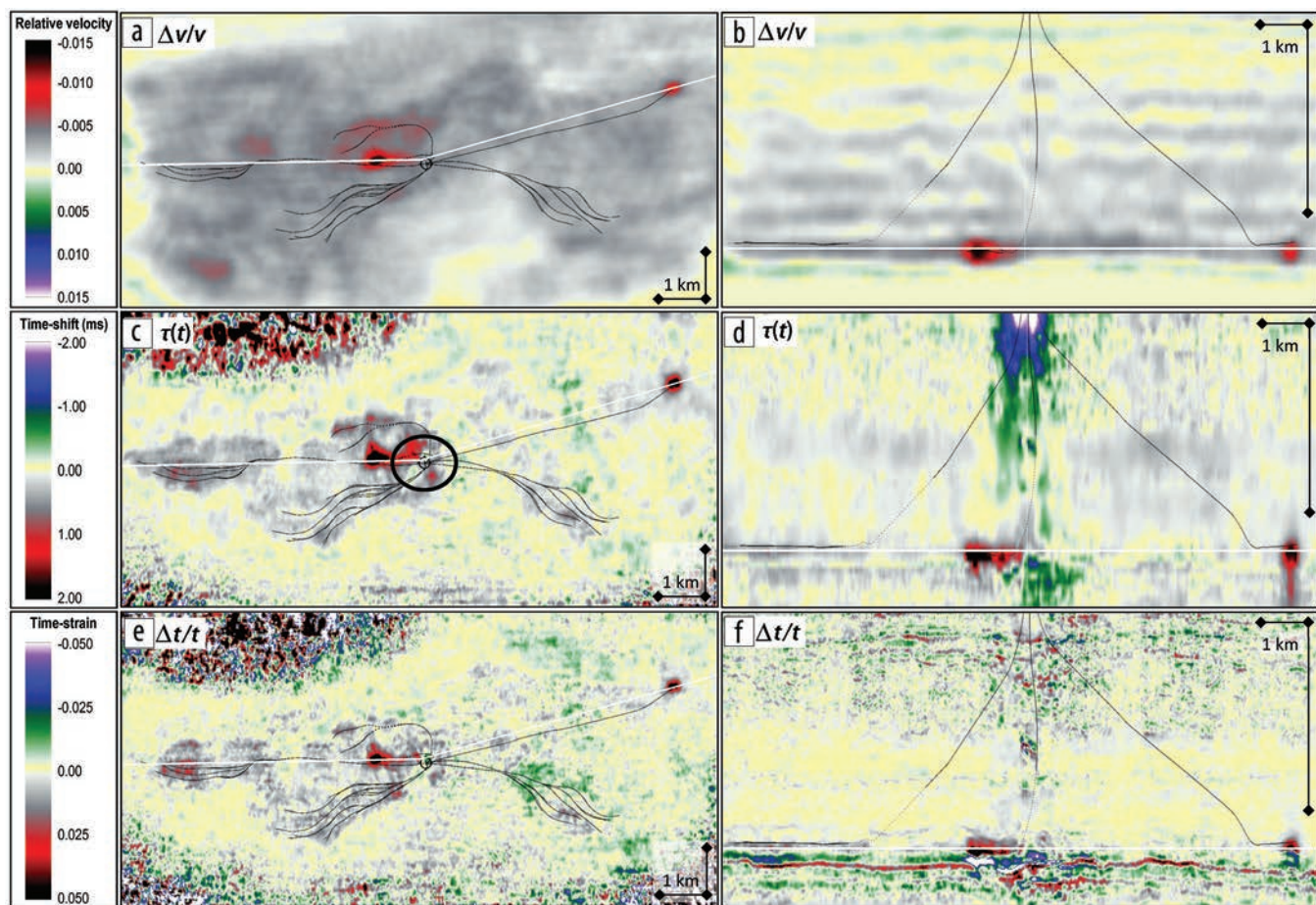

Figure 9. Results from the Grane PRM real-data study: (a) relative velocity change, $\Delta v/v$, from the common-model 4D FWI, (c) time-shifts, $\tau(t)$, and (e) time strains, $\Delta t/t$, from migrated stacks on a depth slice at the reservoir level; (b) relative velocity change from common-model 4D FWI, (d) time shifts, and (f) time strains from migrated stacks on a vertical section through the two main reservoir anomalies. Note that the color scale is reversed for time shifts and strains (c)–(f) to accommodate the opposite sign. The thin white line on the depth slices in (a), (c), and (e) indicates the position of the vertical section, and vice versa with (b), (d), and (f). The black circle in (c) is the location of the platform. Well paths of some active producers/injectors during the six-month interval are shown.

with the traditional time-strain analysis is a first in the industry. Future work includes comparing these results to a fully coupled, joint 4D FWI inversion scheme. **TLE**

Corresponding author: erik.hicks@cgg.com

References

Asnaashari, A., R. Brossier, S. Garambois, F. Audebert, P. Thore, and J. Virieux, 2012, Time-lapse imaging using regularized FWI: a robustness study: 82nd Annual International Meeting, SEG, Expanded Abstracts, http://dx.doi.org/10.1190/segam2012-0699.1.

Asnaashari, A., R. Brossier, S. Garambois, F. Audebert, P. Thore, and J. Virieux, 2015, Time-lapse seismic imaging using regularized full-waveform inversion with a prior model: which strategy?: Geophysical Prospecting, **63**, no. 1, 78–98, http://dx.doi.org/10.1111/1365-2478.12176.

Chen, G., P. Routh, A. Mullur, P. Singh, X. Lu, M. Helgerud, S. Lazaratos, S. Adamson, D. Jonhston, and S. Zantout, 2015, Application of full wavefield inversion to deep-water 4D seismic surveys — Workflow and analysis of the results: 77th Conference and Exhibition, EAGE, Extended abstracts, http://dx.doi.org/10.3997/2214-4609.201412554.

Denli, H., and L. Huang, 2009, Double-difference elastic waveform tomography in the time domain: 79th Annual International Meeting, SEG, Expanded Abstracts, 2302–2306, http://dx.doi.org/10.1190/1.3255320.

Elde, R. M., S. Sinha Roy, C. F. Andersen, and T. Andersen, 2016, Grane permanent reservoir monitoring — Meeting expectations!: 78th EAGE Conference and Exhibition, EAGE, Extended Abstracts, http://dx.doi.org/10.3997/2214-4609.201600573.

Etgen, J., 1986, High-order finite-difference reverse time migration with the 2-way non-reflecting wave equation: Stanford Exploration Project, report SEP-48, 133.

Gardner, G.H.F., L.W. Gardner and A.R. Gregory, 1974, Formation velocity and density — the diagnostic basics for stratigraphic traps: Geophysics, **39**, no. 6, 770–780, http://dx.doi.org/10.1190/1.1440465.

Hatchell, P., and S. Bourne, 2005, Rocks under strain: Strain-induced time-lapse time shifts are observed for depleting reservoirs: The Leading Edge, **24**, no. 12, 1222–1225, http://dx.doi.org/10.1190/1.2149624.

Lebedev, V. I., 1964, Difference analogues of orthogonal decompositions of basic differential operators and some boundary value problems: I: U.S.S.R. Computational Mathematics and Mathematical Physics, **4**, no. 3, 69–92, http://dx.doi.org/10.1016/0041-5553(64)90240-X.

Lescoffit, S. P., M. Houbiers, C. Henstock, E. Hicks, H. Hoeber, K.-M. Nielsen, A. Ratcliffe, and V. Vinje, 2016, Time-lapse full-waveform inversion applied to permanent reservoir monitoring data from Grane, a Norwegian North Sea field: 86th Annual International Meeting, SEG, Expanded Abstracts, 1304–1308, http://dx.doi.org/10.1190/segam2016-13905060.1.

Lisitsa, V., and D. Vishnevskiy, 2010, Lebedev scheme for the numerical simulation of wave propagation in 3D anisotropic elasticity: Geophysical Prospecting, **58**, no. 4, 619–635, http://dx.doi.org/10.1111/j.1365-2478.2009.00862.x.

Maharramov, M., and B. Biondi, 2014, Joint full-waveform inversion of time-lapse seismic data sets: 84th Annual International Meeting, SEG, Expanded Abstracts, 954–959, http://dx.doi.org/10.1190/segam2014-0962.1.

Plessix, R.-E., S. Michelet, H. Rynja, H. Kuehl, C. Perkins, J. W. de Maag, and P. Hatchell, 2010, Some 3D applications of full waveform inversion: 72nd Conference and Exhibition, EAGE, Workshops and Fieldtrips, Session: WS6 3D Full Waveform Inversion – A Game Changing Technique?

Raknes, E., W. Weibull, B. Arntsen, 2013, Time-lapse full waveform inversion: Synthetic and real data examples: 83rd International Meeting, SEG, Expanded Abstracts, 944–948, http://dx.doi.org/10.1190/segam2013-0540.1.

Routh, P., G. Palacharla, I. Chikichev, and S. Lazaratos, 2012, Full wavefield inversion of time-lapse data for improved imaging and reservoir characterization: 82nd Annual International Meeting, SEG, Expanded Abstracts, 1-6, http://dx.doi.org/10.1190/segam2012-1043.1.

Sinha Roy, S., F. Bøen, A. Sæbø, and S. I. Aanonsen, 2011, 4D seismic monitoring — A case study on the Grane Field, North Sea: 73rd EAGE Conference & Exhibition, EAGE, Extended Abstracts, http://dx.doi.org/10.3997/2214-4609.20149227.

Sinha Roy, S., C. F. Andersen, A. Sæbø, and F. Bøen, 2015, 4D seismic in Grane — Adding value over generations: 77th EAGE Conference and Exhibition, EAGE, Extended Abstracts, http://dx.doi.org/10.3997/2214-4609.201413158.

Tarantola, A., 1984, Inversion of seismic reflection data in the acoustic approximation: Geophysics, **49**, no. 8, 1259–1266, http://dx.doi.org/10.1190/1.1441754.

Thompson, M., M. Andersen, R. M. Elde, S. S. Roy, and S. M. Skoglund, 2015, Delivering permanent reservoir monitoring for Snorre and Grane: Third Workshop on Permanent Reservoir Monitoring, EAGE, http://dx.doi.org/10.3997/2214-4609.201411980.

Thomsen, L. A., 1986, Weak elastic anisotropy: Geophysics, **51**, no. 10, 1954–1966, http://dx.doi.org/10.1190/1.1442051.

Watanabe, T., S. Shimizu, E. Asakawa, and T. Matsuoka, 2004, Differential waveform tomography for time-lapse crosswell seismic data with application to gas hydrate production monitoring: 74th Annual International Meeting, SEG, Expanded Abstracts, 2323–2326, http://dx.doi.org/10.1190/1.1845221.

Zhang, Z., and L. Huang, 2013, Double-difference elastic-waveform inversion with prior information for time-lapse monitoring: Geophysics, **78**, no. 6, R259–R273, http://dx.doi.org/10.1190/geo2012-0527.1.

Zheng, Y., P. Barton, and S. Singh, 2011, Strategies for elastic full waveform inversion of time-lapse ocean bottom cable (OBC) seismic data: 81st Annual International Meeting, SEG, Expanded Abstracts, 4195–4200, http://dx.doi.org/10.1190/1.3628083.